

Enabling Fast-Charging Lithium-Ion Battery Anodes: Influence of Spheroidization on Natural Graphite

Marilena Mancini,^[a] Jan Martin,^[a] Irene Ruggeri,^[a] Nicholas Drewett,^[b] Peter Axmann,^[a] and Margret Wohlfahrt-Mehrens^[a]

Excellent fast-charging performance is a key requirement for lithium-ion batteries intended for automotive applications. Rational particle design for active materials within electrodes represents a strategic approach to minimize kinetic limitations – especially for the anode, where the lithium intercalation rate affects the overall cell charging capacity at elevated current densities. Typically, for practical applications, natural graphite flakes are shaped into rounded particles via a mechanical spheroidization process. In this work, we show that both surface and bulk particle properties correlate strongly with the applied

spheroidization conditions, and directly affect the electrochemical performance, particularly in terms of lithium-intercalation rate. We demonstrate that graphite particles with a surface rich in prismatic planes, structural defects, and oxygen-rich groups are favorable for fast lithium uptake. The influence of the graphite particle characteristics on the lithium intercalation rate plays a key role at the electrode and cell level, affecting the overall cell performance. We provide new insights into particle optimization during spheroidization as an effective strategy for developing fast-charging lithium-ion batteries.

Introduction

Lithium (Li) ions can intercalate electrochemically between the graphene layers of the graphite structure through its prismatic planes, leading to the formation of the lithium-graphite intercalation compounds (Li-GICs). Under ambient conditions, lithium intercalation occurs up to the maximum theoretical composition of LiC₆ at potentials very close to that of metallic lithium. These unique electrochemical properties, along with abundance and non-toxicity, made graphite the natural choice as anode active material in Li-ion batteries (LIBs) for over 30 years. Although other active material families with larger specific capacities may be used, frequently this is offset by specific drawbacks. For example, next to graphite, one of the most commonly used active material is silicon, which offers high specific capacity but suffers from poor cycling stability due to well-known volume expansion related issues. This limits the amount of silicon that can be used in the electrode composition, and so it is frequently employed in conjunction with graphite in composite anodes. Consequently, increasing graphite demand is expected in the near future driven mainly by the impressive market growth of LIBs, especially in the

automotive sector.^[1] For such applications, a short charging time is as important as energy density, safety, long cycle life, and low-cost. The large-scale electrification of transport vehicles and their market penetration require reducing the charging time of LIBs in EVs (e.g., less than 20 min) to be comparable with refuelling time of combustion engine cars. Besides the intrinsic kinetics of the lithiation/de-lithiation process of the active materials, the charging rate of a Li-ion cell depends on many factors at different levels, encompassing all steps from the electrode manufacturing methods to the cell charging procedure. Therefore, fast-charging performance can be achieved with optimization of the overall cell design and components including active and non-active materials, electrode architecture, separator and electrolyte.^[2–8] At the electrode level, reduced mass loading generally improves the rate performance at the expense of energy density. Hence, electrode properties (such as loading, porosity, density, electric conductivity and tortuosity) need to be tailored carefully to meet both requirements of fast kinetics and high energy density.^[3,8] Another parameter that directly influences the charging rate of a Li-ion cell is the choice of the electrolyte system. Ideally, the lithium ion transport has to be fast enough to avoid lithium depletion in the liquid electrolyte phase near to the anode surface under demanding charging conditions, such as high current rates.^[2] Provided that lithium ions are readily available at the anode side, sites for intercalation need to be easily accessible at the graphite surface. When this overall process is inhibited, anode polarization occurs with consequent undesired side-reactions (such as lithium plating and dendrite formation, and consequent safety risks).^[5] At the interface between the liquid electrolyte and the graphite, the charging process comprises of very complex intermediate steps (desolvation of the lithium ions, their migration through the solid electrolyte interface – SEI, access to the edge-planes of the

[a] Dr. M. Mancini, J. Martin, Dr. I. Ruggeri, Dr. P. Axmann, Dr. M. Wohlfahrt-Mehrens
Accumulator Materials Research (ECM)
Zentrum für Sonnenenergie- und Wasserstoff-Forschung
Baden-Württemberg (ZSW)
Helmholtzstraße 8, 89081 Ulm, Germany
E-mail: marilena.mancini@zsw-bw.de

[b] Dr. N. Drewett
Centre for Cooperative Research on
Alternative Energies (CIC energiGUNE)
Basque Research and Technology Alliance (BRTA)
Alava Technology Park, Albert Einstein 48,01510 Vitoria-Gasteiz, Spain

 Supporting information for this article is available on the WWW under
<https://doi.org/10.1002/batt.202200109>

graphite structure, and finally intercalation between the graphene layers into the graphite bulk), each with specific reaction kinetics.^[6,7] Indeed, many studies have suggested that the lithium intercalation process and its related kinetics are the main factors determining the fast-charging ability of the whole battery system.^[8–10] Even though the mechanism of interface reactions and the rate-determining step of the lithium intercalation reaction remain partly unclear due to their complexity, the importance of the carbon surface is well established.^[6] The considerable advances made in the field of characterization techniques, along with the increasing quality standards required for LiB applications, led to a more nuanced understanding of the nano- and micro-scale properties to target when optimizing graphite as an active material.

The industrial production of natural graphite for LiBs applications involves several steps, starting with extraction of the mineral, followed by processing (such as grinding and purification), and finishing with the refinement of the final product.^[11] Currently, the market offers a variety of graphite for LiBs applications, where various production steps (such as shaping, coating, and surface treatments) are employed to ensure quality (e.g., carbon coating of the graphite particles in order to reduce surface area and further increase conductivity). However, the increasing demand for high energy density under stressful operative conditions (such as low temperatures and high charging current densities) represents a significant challenge for standard graphite anodes. In order to improve the anode rate capability, literature reports a range of different approaches to create intercalation sites at the surface of the graphite (such as chemical etching with alkali treatment, exfoliation of graphite edges via edge-selective functionalization, thermal oxidation, etc.).^[12–15] Other strategies reported to increase anode kinetics focus on the design and modification at the electrode level, such as alignment of graphite flat particles by applying a low-magnetic field to reduce electrode tortuosity, or coating the electrode surface with thin metal layers to improve electrode/electrolyte interfacial kinetics.^[16–18] Even when these approaches can be applied on a large scale, they require additional treatment steps or equipment, either during the production of the active material or during the electrode manufacturing process, compared to standard LiB production. Consequently, from a practical point of view, improved understanding of the state-of-the-art production of graphite powder and its impact on the electrochemical performance is of strategic importance. One of the most important steps during the production of natural graphite for LiBs anode is the spheroidization. Typically, the original flake-like particles – with relatively large aspect ratio and low density – are shaped mechanically into nearly spherical particles with relatively low surface area and increased density.^[19] Compared to flakes, the rounded graphite particles not only offer easier processability during electrode manufacturing, but also reduced electrode tortuosity, which determines the effective electrolyte conductivity and diffusivity of the porous electrode and is crucial for rate-performance of the anode. In addition, at the particle level, spherical shape facilitates homogenous lithium intercalation compared to flat graphite flakes. Flakes

tend to align themselves along the current collector direction during standard coating process. Such a particle orientation hinders fast access of lithium ions to the intercalation sites, which are present mainly at the edges of the flat particles. During the spheroidization, the breaking and folding of the big natural graphite flakes occurs with the formation of a large number of surface defects.^[20–22] The resulting morphological, physical, and chemical properties of the particle surface influence both reversible and irreversible (due to SEI formation) electrochemical reactions at the interface between the active material and the liquid electrolyte. The choice of the spheroidization parameters, and thus the energy involved during the milling process, influences not only the morphology but also the open and closed particle porosity.^[23] Examination of the literature reveals different examples of shaping processes for obtaining rounded graphite particles.^[20–25] However, the influence of the shaping parameters on the particle characteristics, which control the fast-charging performance of the anode, has, to the best of our knowledge, currently not been reported.

With the aim of developing a rational design approach for graphite particles to be used in LiBs, this study investigates the fast-charging ability of spheroidized natural graphite samples produced with different milling parameters and characterized as model systems for a comparative analysis. In a recent paper, we demonstrated that the lithiation kinetics of the anodes based on spheroidized graphite depends on the availability of surface defects and prismatic planes, which are associated with reduced charge-transfer resistance.^[22] For a better understanding of the correlation between graphite spheroidization conditions and intercalation rate, in the present work we demonstrate that the particle characteristics induced by the shaping process significantly affect the overall fast-charging performance of the anode in practical applications, i.e., in model full cells with commercially valid specifications. We investigate the complex nature of the carbon surface, including surface heterogeneities and structural defects, by means of several analytical techniques to reveal direct correlation between the spheroidization treatment and the electrochemical behaviour and to provide new insights for graphite design principles.

Results and Discussion

We milled the original flakes of natural graphite via a lab-scale spheroidization process. During treatment in the high-speed rotational dry impact mill, the continuous impact of the graphite flakes against the rotor/stator and other particles leads to the formation of the rounded particles. The characteristic of the final powder depends on the applied spheroidization conditions. In addition to batch size, the energy involved during the process is directly proportional to milling time and rotation speed. Generally, increasing milling energy leads to smaller and more spherical particles, and concurrently to an increase in specific surface area due to the formation of larger amounts of fine particles ("milling effect"), which may finally re-attach on the graphite spheres. The range of the particle

diameter was controlled via sieving and classification of the powder obtained after the spheroidization treatment, in order to obtain a narrow particle size distribution. The final graphite samples, named NG1 and NG2, result from relatively low (9000 rpm/4 min) and high-impact milling conditions (11000 rpm/8 min), respectively. The two samples have been sieved and classified using the same experimental conditions to obtain comparable particle size distribution before further characterization. The particle size distribution used in this work was selected according to typical values of commercial graphite samples for LiBs applications.^[23] Figure 1 shows the particle morphology of the two samples. After the milling treatment, both NG1 and NG2 show potato-like particles resulting from the folding of the pristine flakes into rounded particles with smooth edges, confirming that the applied lab-scale method allows effective shaping of the graphite flakes. However, morphological differences between the two samples are observed and ascribed to the different milling conditions used for the rounding process.

Due to the higher spheroidization energy, the NG2 particles exhibit a smoother surface and more spherical and uniform

morphology compared to NG1. The smaller NG1 particles in particular look partly flat and with a rougher surface. Besides surface morphology, several physical properties were measured with different analytical methods and summarized in Table 1. After sieving and classification, slightly smaller particle size values were obtained for NG2 compared to NG1. This is expected due to the higher rotation speed and longer milling time, leading to slightly reduced particle diameter and more spherical particles that facilitate sieving separation. Measured bulk and tap density values are higher for the NG2 than NG1 powder, which is consistent with the more spherical morphology enabling better packing. Furthermore, the higher the energy involved during the milling, the higher the possibility of surface cracks (and re-attachment of small fragments of the graphite flakes onto the particle surface), which increases the surface area. Accordingly, the total specific surface area, calculated from N₂ physisorption with the Brunauer-Emmett-Teller (BET) theory, is ca. 7 and 12 m²g⁻¹ for NG1 and NG2, respectively.

To elucidate information regarding the nature of the carbon particles near-surface regions, and any changes resulting from

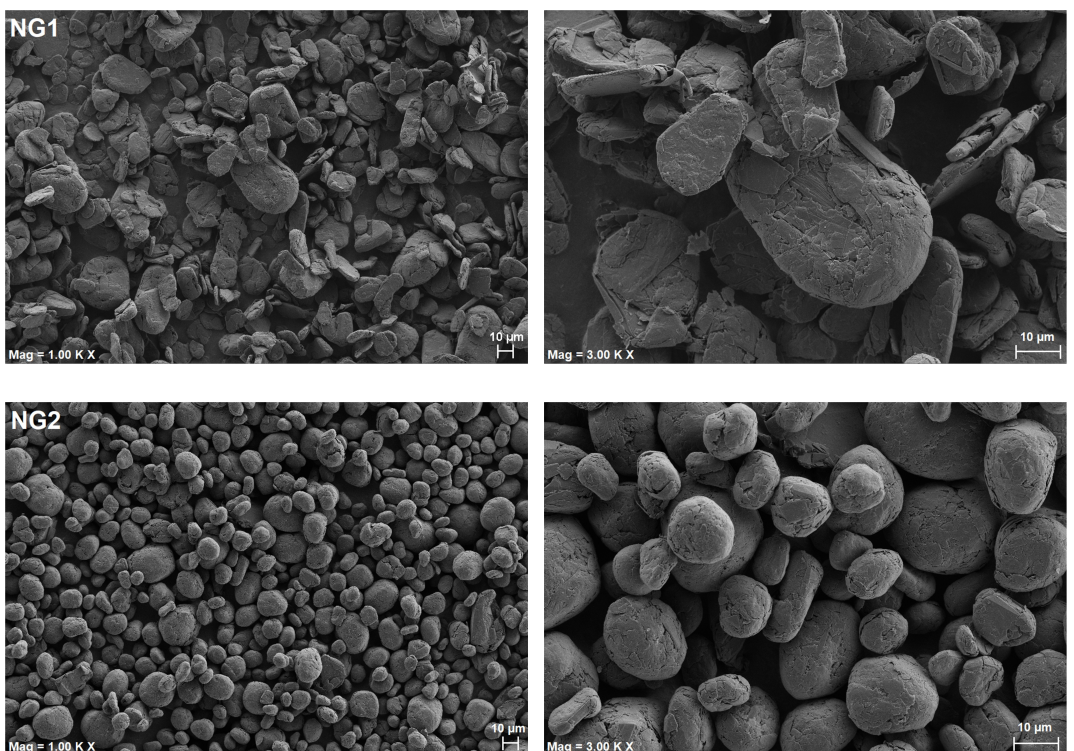


Figure 1. SEM images of graphite NG1 (top) and NG2 (bottom) after milling, sieving and classification.

Table 1. Summary of the characterization results from different methods of the samples NG1 and NG2.

	Bulk density [g L ⁻¹]	Tap density [g L ⁻¹]	Particle size distribution $d_{10}/d_{50}/d_{90}$ [μm]	Specific surface area [m ² g ⁻¹]	I_D/I_G	L_a [nm]	Prismatic surface area [%]	Basal surface area [%]	Defect surface area [%]
NG1	568	826	11/21/39	7	0.31	72	21.9	58.1	20.0
NG2	697	929	9/15/27	12	0.55	46	48.8	33.2	18.0

the spheroidization process, Raman spectra were collected from NG1 and NG2 and analysed. Figure 2 shows typical spectra for these materials.

From these datasets, the following peaks were identified and assigned: the first order spectra (observable between 1000 and 2000 cm^{-1}), consisting of the D-band (ca. 1350 cm^{-1}), the G-band corresponding to E_{2g} mode of the sp^2 -carbon network (ca. 1580 cm^{-1}) and the D' visible as a small shoulder on the higher frequency side of the G-band (ca. 1615 cm^{-1}). The second order spectra (observable between 2000 and 3500 cm^{-1}) consist of the G' band (ca. 2500–2800 cm^{-1} , sometimes also referred to as the 2D band as it corresponds to the overtone of the D-band), the combination modes D+D'' (ca. 2500 cm^{-1}) and G+D (ca. 2920 cm^{-1}), and 2D' (ca. 3200 cm^{-1} , which corresponds to the overtone of the D' band).^[26–29] The G band is associated with the longitudinal optical (LO) phonon mode, while the D and D' bands result from defect-induced Raman.^[29] Thus, the integrated intensity ratio I_D/I_G for the D band and G band represents a good indicator for determining

the in-plane crystallite size or characterizing the defect quantity and degree of disorder in graphitic materials.^[30,31] Consequently, peak fitting was carried out on the collected Raman spectra (see Figures S2 and S3) to enable extraction of the relevant data. The I_D/I_G ratios and peak positions correlate well with those previously reported in the literature, corresponding to Stage 1 disorder.^[32] However, key differences between the NG1 and NG2 samples were apparent – most notably, in the distribution of particles with a greater degree of defects and disorder. In order to facilitate a representative comparison between the two graphite samples, the frequency distribution of particles with calculated intensity ratios I_D/I_G was plotted from spectra obtained for NG1 and NG2 (see Figure 3).

As it can be seen from this analysis, spheroidization results in the I_D/I_G ratio distribution shifting to higher values comparative to the pristine materials (see Figure S4 in Supporting Information), which may be attributed to increasing disorder and defects being introduced as a result of the milling process.^[33–35] Notably, the spectra of NG2 exhibit much higher I_D/I_G ratio values and a much broader distribution compared to those of NG1. The mean I_D/I_G value was found to be 0.31 for NG1 and 0.55 for NG2, and the calculated values for the L_a crystallite sizes were 72 and 46 nm for NG1 and NG2, respectively. In general, Raman results indicate that the NG2 particles show a greater degree of defects and disorder compared to those of NG1, which may be attributed to higher energy involved in the NG2 spheroidization process resulting from the differences in milling conditions (i.e., higher rotation speed and milling time). In this way, this strongly supports the possibility of tuning graphite disorder and defects based on selection of spheroidization process parameters. To probe the differences between the two materials still further, physisorption and chemisorption techniques were employed to gain insights into the nature of their respective surfaces. Given that the shaping process applied influences the disorder and defects observed, it is important to establish if it also significantly influences the type and amount of surface groups on the particles – particularly since the reactivity of the surface chemistry may very strongly affect the electrochemical behaviour of carbon-based anodes. The surface area calculated with the BET theory from nitrogen physisorption alone does not take into account the differences in the surface types that the carbon generally presents due to a variety of defects and deviation from the ideal structure. Therefore, we performed the analysis of the isotherms by using a well-known NLDFT model based on the difference in the adsorptive potential of nitrogen on heterogenic surfaces.^[36] Based on this model, it is possible to estimate the relative amount of basal, prismatic, and defect surfaces on micro-pore-free carbons.^[37] The calculated values of surface heterogeneity distribution, reported in Table 1, show that the percentage of prismatic surfaces on NG2 particles is significantly higher than for NG1, where the presence of basal planes is instead the dominant feature. The graphite surface chemistry and its reactivity were further investigated by means of oxygen chemisorption and temperature-programmed-desorption coupled with mass spectrometry (TPD-MS). For this analysis, the carbon powders are typically outgassed up to

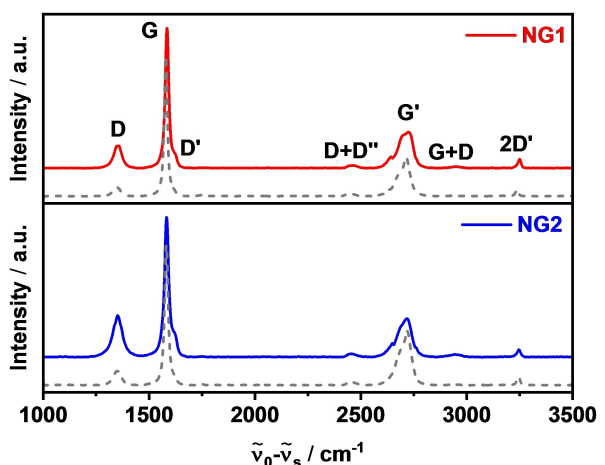


Figure 2. Raman spectra for NG1 and NG2 (dotted lines correspond to the pristine material).

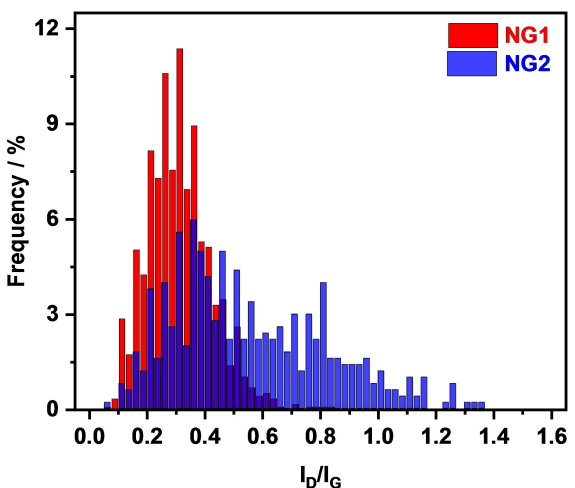


Figure 3. Distribution of the relative frequencies of I_D/I_G ratios from Raman measurements of NG1 and NG2 samples.

1000 °C to remove the species chemisorbed on the surface. The subsequent oxygen chemisorption treatment at 300 °C leads to the formation of new functional groups on the bare graphite surface at specifically reactive carbon sites. During the TPD, the decomposition of such functional groups takes place, and the desorbed species are detected by mass spectrometry. Figure 4 shows the main gas species desorbed during TPD plotted as a function of time and temperature for NG1 and NG2 after oxygen chemisorption.

Both materials show H₂O desorption in the temperature range of 300–500 °C, which can be ascribed to dehydration of oxygenated groups (carboxylic acids or phenols) into anhydrides or lactones. The amount of desorbed CO₂ is very low for both materials, and may be attributed to the decomposition of carboxylic acid, lactones, lactols, or carboxylic anhydrides at temperatures above 400 °C.^[38–39] For both samples, the most intense signal is detected above 500 °C and is ascribed to the production of CO, originating mainly from the decomposition of phenol, ether, and/or carbonyl groups. We tentatively ascribe the CO signal at ca. 700 °C to the decomposition of phenol or anhydrides, and the CO signal at ca. 980 °C to the decomposition of carbonyls, quinones and ethers, in accordance with the literature.^[38–44] At temperatures close to 800 °C some H₂ formation is observed, which has also previously been reported during the graphitization process of graphitizable carbons and is ascribed to re-arrangement of carbon-bonds.^[45] Overall, the TPD analysis reveals that the amount of desorbed gases is

significantly higher for NG2 compared to NG1. This suggests that the reactive surface area, where oxygen-containing groups are formed on the carbon surface from reaction with oxygen, is higher on the NG2 graphite surface. This agrees with the presence of several surface defects and prismatic planes at the NG2 particles. In literature, the surface characterization of carbon by analysis of heterogeneity from nitrogen physisorption and by oxygen chemisorption has been reported for commercial graphite thermal treated under different conditions.^[37–38,46] To the best of our knowledge, this is the first time these methods have been applied to study the impact of spheroidization on natural graphite. Here, we demonstrate that mechanical milling conditions can strongly influence the chemistry of the graphite particles, with the oxygen chemisorption results being consistent with nitrogen physisorption and Raman analysis. This confirms that the higher energy milling conditions used for the spheroidization of NG2 lead not only to higher tap density and surface area, but also to higher amount of surface defects, prismatic surfaces and active sites compared to NG1. The graphite structure is highly anisotropic with respect to lithium diffusion coefficient, which is much higher in the edge-plane direction than in the through-plane direction of graphite layers.^[47] Therefore, the presence of prismatic and defect-rich surfaces is favourable for fast lithium intercalation. Recently, we studied the interface kinetics of anodes made with NG1- and NG2-type graphite materials by extended electrochemical impedance spectroscopy investigation, and demonstrated faster kinetics and reduced charge-transfer resistance for the NG2-type graphite electrodes.^[22] However, from a practical perspective, it is important to assess how the properties of the graphite active material influence the electrochemical performance with respect to real applications. To fully understand how the conditions used for graphite spheroidization may affect the LiB performance, in this work the graphite samples are investigated electrochemically at different levels: i) as active materials in electrodes with relatively low mass loading, ii) in electrodes with state-of-the-art mass loading and density, and iii) in full-cells with commercially valid configuration vs. standard NCM-based cathode. We applied selected cycling procedures and data analysis with a focus on fast-charging applications. The two graphite samples were processed into electrodes with compositions typical of commercially available anodes via a standard water-based slurry preparation. Two types of electrodes have been fabricated: electrodes with small active material loading (ca. 3 mg cm⁻², not calandered) and "standard" electrodes with state-of-the-art active material loading (ca. 8 mg cm⁻² and calandered to 1.4 g cm⁻³ density). In electrodes with very small mass loading, the thickness corresponds to 2–3 times the average diameter of the rounded particles and therefore the electrodes consist of a few graphite layers. These conditions allow minimization of the kinetic limitations typically associated with standard electrode parameters (tortuosity, density, porosity) and with the use of metallic lithium as counter electrode (limited by the kinetics of lithium stripping and deposition at high current densities).^[48] Therefore, we can directly correlate the electrochemical performance with the active material properties. In standard electrodes, with

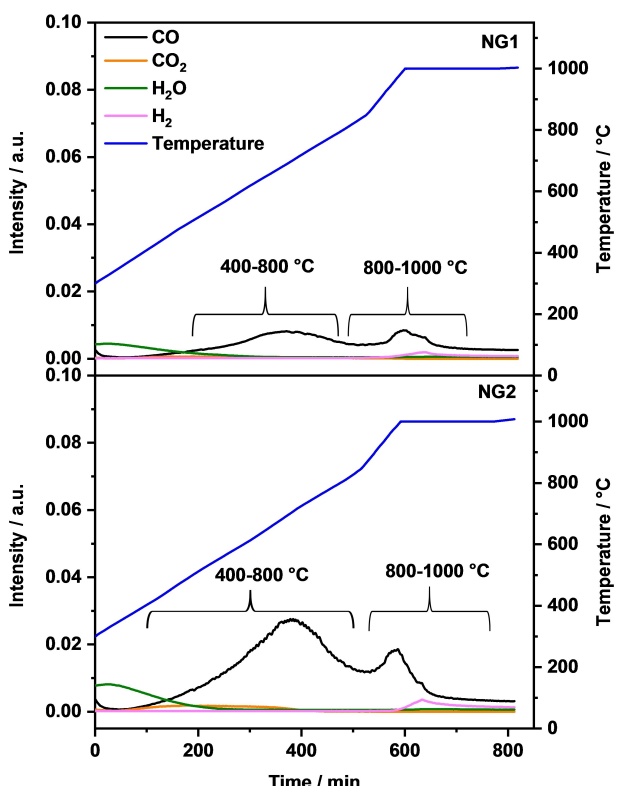


Figure 4. Intensity versus time of mass spectra signals of CO, CO₂, H₂O and H₂ detected during TPD-MS analysis of NG1 and NG2 samples. Temperature ranges of most intense CO signals are also reported.

higher mass loading and density, specific parameters such as porosity and tortuosity have a strong effect on the fast-charging performance besides the properties of the active material.^[3,8] Both electrode types were tested in half-cells vs. metallic lithium by using state-of-the-art electrolyte. During the first cycle, most of the irreversible reactions associated with the formation of the SEI take place. The specific irreversible capacity loss at the first charge/discharge cycle is significantly higher for NG2 compared to NG1 (e.g., 68 and 47 mAh g⁻¹ for NG2 and NG1 standard electrodes, respectively). As expected, the irreversible capacity increases with increasing of the surface area. Besides the total surface area, the carbon surface characteristics described above in terms of defects, reactivity, and prismatic/basal planes distribution also strongly affect the SEI formation mechanism, composition, and stability. Indeed, the reductive decomposition of most common electrolyte solvents takes place mainly at the prismatic planes of the graphite surface, where the lithium intercalation occurs.^[49] Therefore, a larger total surface area and higher amount of prismatic surface would naturally correlate with a larger consumption of lithium to form the SEI. On the other hand, the presence of oxygen-rich surface groups, as in the case of the NG2 sample, is generally favorable for promoting effective SEI composition (in terms of stability and conductivity).^[50] Although the study of the SEI stability as a function of the carbon surface chemistry is beyond the scope of this work, and will be the subject of a further paper, it bears mentioning here in order to highlight the necessity of balancing such factors. After the initial formation cycles, the electrodes were lithiated galvanostatically using different current densities (constant current, CC)

and de-lithiated at a relatively slow rate (i.e., 0.2 C). At the end of each galvanostatic lithiation, a potentiostatic (constant voltage, CV) step at 0.02 V vs. Li/Li⁺ was applied. During the CV step, the maximum degree of lithium intercalation to the composition of ca. LiC₆ is forced by the applied potential with no time limitation. This cycling protocol corresponds to a CCCV charging and CC discharging mode in a full-cell configuration.^[3,4] By applying the CCCV lithiation method described above, both NG1 and NG2 electrode types can be lithiated up to the maximum theoretical capacity of 372 mAh g⁻¹, independently from both the electrode loading and density and the CC rate. However, the amount of lithium stored under galvanostatic conditions (CC capacity) depends on the electrode parameters and on the graphite used, as expected. Figure 5 shows the comparative analysis of the voltage profiles recorded during the CC lithiation step at different current rates for the thin electrodes.

With increasing current rate, the voltage shifts towards lower values due to polarization, as expected. This leads to a decreased amount of stored lithium, as the reduction cut-off voltage of 0.02 V vs. Li/Li⁺ is reached before the electrochemical intercalation to form LiC₆ is completed. Consequently, the CC specific lithiation capacity decreases and the duration of the CV step increases with increasing current rate. At relatively low CC rates (i.e., 0.2 C), the voltage profiles of the two types of anodes are very similar. Accordingly, for both types of electrodes the specific CC capacity is very close to the maximum theoretical capacity. At higher current rates, the polarization of NG1-type electrodes is significantly more pronounced than for NG2-type, leading to a shift of the voltage plateaus to lower

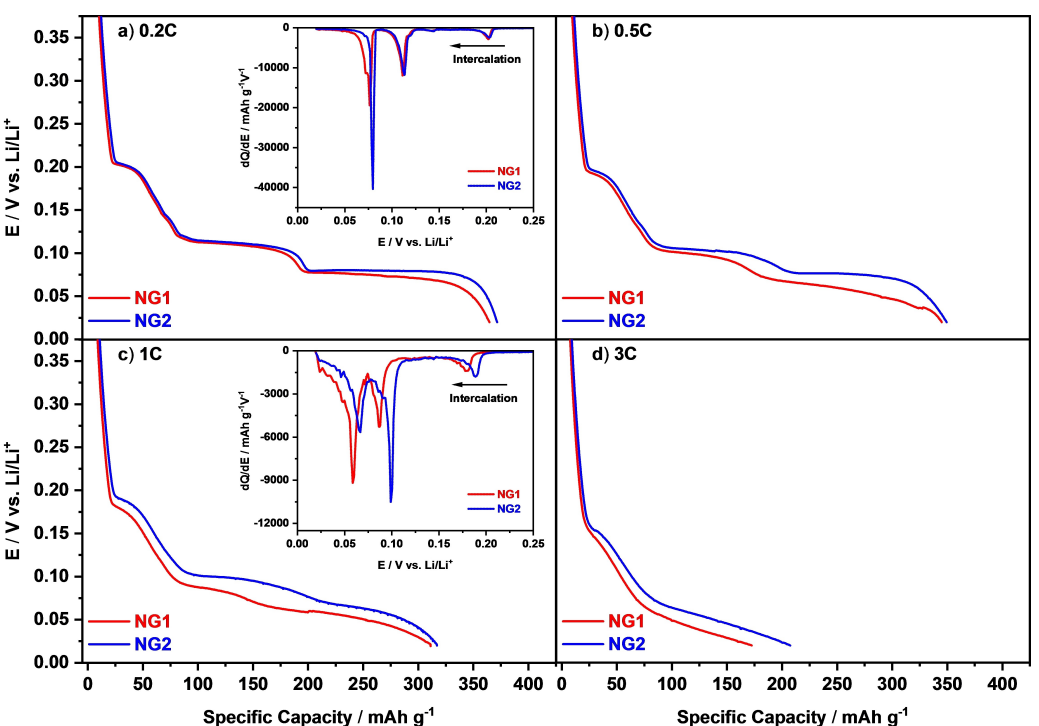


Figure 5. Comparison between lithiation voltage profiles of NG1- and NG2-based anodes (low-loading) at different CC rates. Derivatives of the curves at 0.2 C and 1 C CC rate are plotted in the insets of a) and c), respectively.

values (see derivative analysis in Figure 5a and c) and consequently to a smaller capacity. In order to benchmark the materials in terms of fast-charging performance, thin electrodes made with different commercially available graphite with similar morphology and particle size distribution, have been tested under the same conditions. Although the correlation between material production and electrochemical performance cannot be extended to commercial materials, the NG2 charging behaviour is similar or even superior (see Figure S5 in Supporting Information).

The two spheroidized graphite samples were further tested in electrodes designed to possess state-of-the-art values of capacity (ca. 3 mAh cm⁻²) and density (ca. 1.4 g cm⁻³). The specific lithiation capacity vs. cycle number at increasing current rates for NG1 and NG2 thin (low loading) and standard (higher loading) electrodes is reported in Figure 6a and b, respectively.

As expected, at low current densities, there is no significant difference between the two electrode types, and both graphite samples can be galvanostatically lithiated to form compositions close to LiC₆. At current rates higher than 0.33 C, the specific

capacity values obtained for standard electrodes are significantly smaller than those obtained with thinner anodes. This is attributed to the kinetic limitations of denser and thicker electrodes.^[3,8] Moreover, at high current densities the stripping of the lithium from the counter electrode also has sluggish kinetics. Therefore, limited storage capacity can be obtained at 1 C rate, and negligible capacity is recorded at 3 C (Figure 6b). Nevertheless, the trend observed for thin electrodes is clearly retained when using electrodes with a standard loading and density. At a CC rate of 1 C, standard anodes made with NG2 show more than 30% higher lithiation capacity than NG1. These results are consistent with previously reported data, and suggest a faster kinetics for lithium intercalation for graphite spheroidized by using relative high energy, such as NG2.^[22] The parameters (rotation speed, batch size and milling time) selected for rounding natural graphite flakes have a significant impact on the anode performance under kinetically limiting conditions, such as high charging rates. While other effects, such as a slightly smaller average particle dimension, may synergistically enhance performance, it seems reasonable to ascribe the faster lithium intercalation for NG2 graphite mainly to surface properties, such as the presence of a large number of prismatic and defect-rich surfaces. Indeed, during charging under kinetically limiting conditions, the lithium ions accumulate on the anode particle surface, and the presence of intercalation sites (prismatic surfaces and defects at the graphite structure) becomes the determining factor for the charge transfer rate. To assess the impact of the spheroidized graphite active material properties on fast-charging performance at a cell level, NG1 and NG2 electrodes with benchmark loading and density have been tested in larger cells vs. a NCM-based cathode, by using state-of-art separator and electrolyte. Identical experimental conditions were applied to allow direct comparison between the two anode model systems. After the formation, the cells with ca. 0.05 Ah initial capacity were cycled by using a CCCV charge and CC discharge, with 4.2 V and 3.0 V as cut-off voltages. In order to ensure complete anode lithiation before subsequent discharge, the CV step at 4.2 V was performed with a current limitation of 0.05 C. It is worth noting that CCCV charging protocol is a conventional cycling procedure for LiBs and was not optimized in the present work for the fast-charging applications. Figure 7 shows the comparison of the cell performance in terms of charge capacity vs. cycle number at increasing charging rates. For better understanding of the kinetics of the systems, the charge capacity has been plotted by separating the two contributions to the total charge capacity: the capacity stored during CC step and the contribution due to the CV step at the end of the charge. The plot shows the evolution of the CC and of the CV charge contributions, as a percentage of the initial total (CCCV) charge capacity at 0.2 C, with increasing the charging rate to 0.33 C, 0.5 C, 1 C and 2.5 C. Finally, the cells were further cycled at 0.2 C CCCV to check the capacity retention after the fast-charging cycles. Assuming no differences due to cathode, separator, electrolyte, and cell configuration, as the conditions are the same for both types of cells, the differences observed can be ascribed purely to the graphite type used.

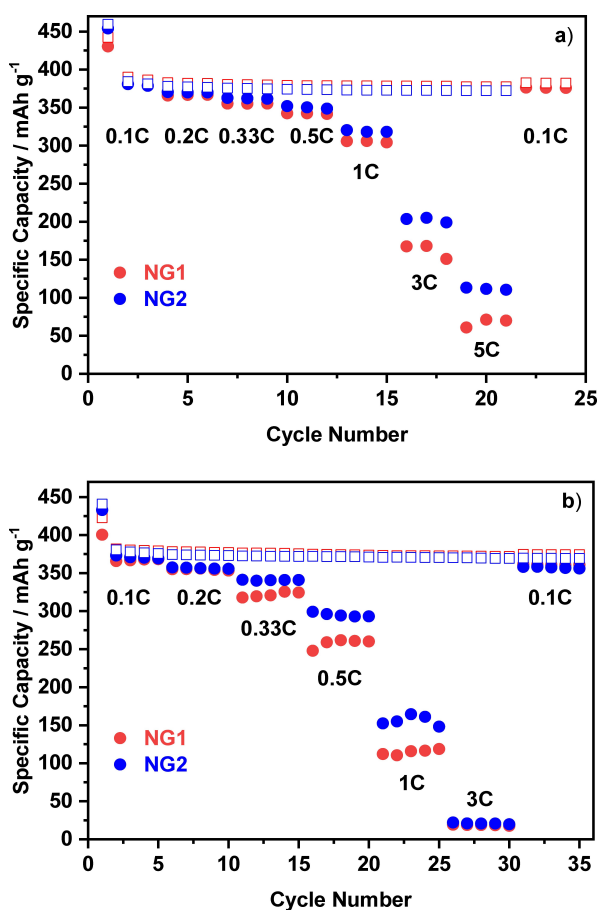


Figure 6. Specific capacity during lithiation of NG1- and NG2-based electrodes at different CC rates in half-cells vs. Li: a) thin electrodes (active material loading of ca. 3 mg cm⁻²) and b) standard electrodes (active material loading of ca. 8 mg cm⁻² and 1.4 g cm⁻³ density). Bold symbols: lithiation specific capacity during CC step; empty symbols: total lithiation specific capacity, measured with including the potentiostatic step at 0.02 V (CC + CV).

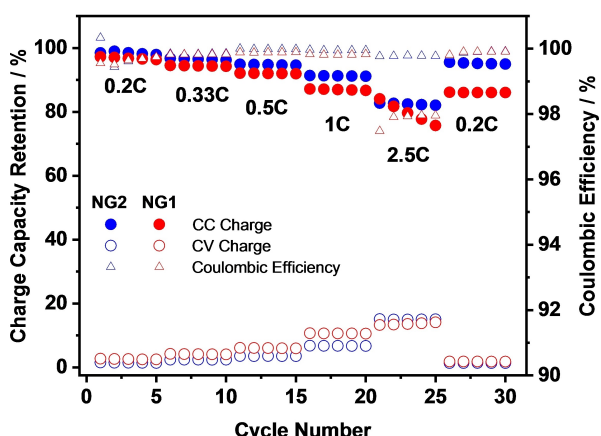


Figure 7. Capacity retention values (CC and CV contributions) as a percentage of the initial total charge capacity and Coulombic efficiency of pouch-cells with anodes based on NG1 (red) and NG2 (blue) graphite.

At relatively low charging rates, both cell types can be charged to almost 100% of the max. capacity under galvanostatic conditions (CC step). At increasing charging rates, the share of the capacity stored during CC step becomes lower for the cells containing NG1 electrodes, leading to an increase of the duration of the CV step. At a charging rate of 1 C, ca. 87% and 91% of the total cell capacity is reached galvanostatically for NG1 and NG2-cells, respectively. The time needed to reach full cell capacity (total charge duration CC+CV) is 1.5 h for NG1 and 1.3 h for NG2 cells. This finding agrees with results obtained in half-cells, suggesting slower kinetics for NG1-type anodes compared to NG2-type. At the charging current of 2.5 C, the NG1-based cells show loss of cycling stability with decreased CC capacity values, accompanied by a decrease of Coulombic efficiency. Under the same conditions, the NG2-based cells show stable CC capacity of 80% of the total capacity with Coulombic efficiency of ca. 100%. By lowering the charging rate to 0.2 C during the last 5 cycles, the cells with the NG1-type graphite show a reduced CC charge capacity (86% of the max. charge capacity) compared to NG2-based cells (95% of max. charge capacity). These results suggest that some side-reaction of irreversible nature occurred at high charging rates for the cells with NG1 anodes leading to capacity loss. It is worth noting that these differences are revealed by applying stressful testing conditions, where ageing phenomena are accelerated especially at the anode side. At lower charging rates (CC 0.2 C), on the other hand, the cycling stability for over 100 cycles (see Figure S6 in Supporting Information) is similar for the two types of cells (96.4% and 95.2% capacity retention after 120 cycles, for NG1 and NG2-based cells, respectively). To better elucidate the influence of the graphite characteristics on the fast-charging performance, more extensive analysis of the electrochemical data acquired during fast-charging conditions is needed. For this purpose, we compared the cell charge/discharge profiles as well as the plots of the current vs. time during the CV step at the end of the charge (4.2 V), recorded during the CCCV charge at different charging currents (see Figure 8). At relatively low charging rates such as 0.5 C, the

charge curves are very similar for the two types of cells (Figure 8a). The discharge profiles (0.2 C) are not affected by the anode as expected. The cell capacity is slightly lower for the NG2 anodes than for the NG1.

This is clearly due to the higher irreversible lithium losses during SEI formation at the first cycle, associated with the larger surface area of NG2 sample, consistently with the half-cells results above described. In fact, the lithium consumed at the anode for SEI building depletes, in full-cells, the amount of lithium available at the cathode for subsequent reversible reactions. Nevertheless, in good agreement with half-cell results, the capacity share during CC charge is higher for NG2 compared to NG1 graphite anodes (Figure 7), indicating that NG2-cells can be charged faster. Consistently, during the following CV step the NG2 anodes show faster current depletion than NG1 (Figure 8b), indicating faster diffusion of the accumulated charges from the surface to the bulk of the anode. During CC charge at 2.5 C (Figure 8c), the galvanostatic profiles reveal more pronounced polarization for NG1 compared to NG2-based cells at potential above 3.5 V. After this step, interestingly, the current vs. time plots recorded during CV period (Figure 8d) reveal two distinct current features for the cells with NG1-anode. The corresponding plot of the cells with NG2-anode shows, on the contrary, the expected behaviour. This result is very important to understand the intercalation kinetics of the anodes. When fast access of the lithium ions into the graphite structure is hindered, the charges accumulate on the carbon surface with risks of lithium reduction. In this way, polarization can be so high at the surface that local deposition of metallic lithium occurs before the lithiation of the graphite is complete. However, in this cell configuration, the information about single electrode voltage cannot be recorded directly as a reference electrode (e.g., metallic lithium) is not present. Therefore, the actual voltage of the anode and the extent of the polarization are unknown. The analysis of the CV step becomes thus important to detect possible interfacial reactions typically occurring during fast charge. In accordance with the slower kinetics of NG1 compared to NG2, the results in Figure 8d can be explained by a second current contribution that may originate from side-reactions beside the pure lithium intercalation. In this case, the intercalation reaction is kinetically limited and the lithium ions accumulate at the interface by creating a charge gradient between the surface and the bulk of the carbon anode. These conditions are likely to occur during fast-charge of the cell and are favourable for local lithium plating, which may re-dissolve during discharge or during relaxation time.^[5,51] It is well-known that when dissolution of plated lithium does not take place, the formation of dendrites and consequent capacity fading and safety risks may occur. During the CV step, the lithium accumulated is forced to intercalate and, in case of local lithium deposition, this latter may eventually re-dissolve and migrate into the graphite bulk. This phenomenon may affect the current plots as shown in Figure 8d.^[52–55] While different methods for detection of lithium plating are described in literature, to the best of our knowledge this is the first time that the analysis of the CV phase is used to study interfacial reactions and reveal possible local lithium plating during fast-charge by using standard CCCV protocol and no reference electrode.^[56,57] Although the analysis method here proposed require further

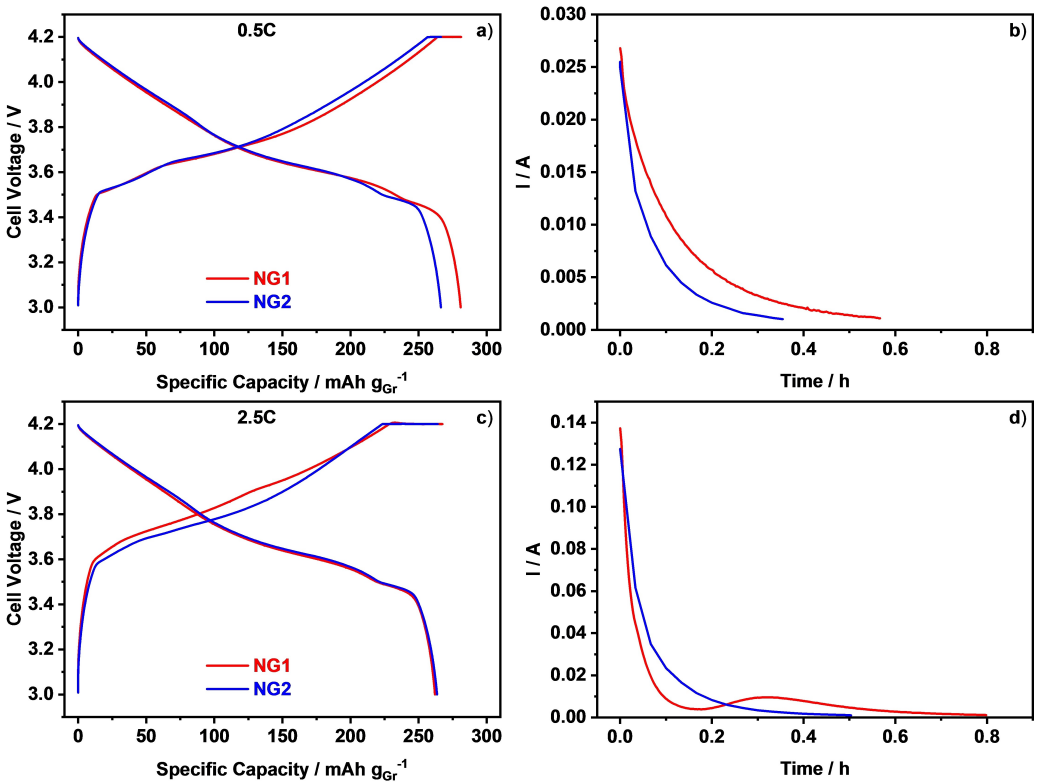


Figure 8. Charge and discharge cell voltages for the two anode types at a) 0.5 C and c) 2.5 C in full-cells; current density decay vs. time during CV period after charging at b) 0.5 C and d) 2.5 C.

understanding, the results support the conclusion that the anode kinetics of spheroidized natural graphite depends on the applied rounding conditions. Moreover, this approach offers a useful tool for early detection of critical conditions associated with lithium deposition initiation and may facilitate in the future the optimization of charging protocols and better understanding of fast-charging performance.

Based on the data interpretation described above, the evaluation of the CV step is fully consistent with the overall electrochemical results already discussed and supports the conclusion that NG1 anodes show lower intercalation kinetics compared to NG2, which is associated with more severe anode polarization under high charging current densities and eventually leads to lithium deposition. Graphite samples such as NG2 possess several synergic characteristics that facilitate fast Li⁺ uptake, such as a large number of prismatic surfaces and defects on the carbon surface, available for Li intercalation; oxygen-rich surface groups that are associated with an efficient SEI; finally, more spherical particles that allow lower electrode tortuosity. All these factors concur to create the conditions for a fast charge transfer at the interface between the carbon and the liquid electrolyte, thus favourable for enabling fast-charging performance. Overall, the electrochemical results and the analytical data for the two graphite example systems corroborate the conclusion that the graphite obtained with spheroidization conditions corresponding to high-energy impact (i.e., higher rotation speed/longer time), such as NG2 sample, may be more favourable for fast-charging applications. This approach represents an opportunity for cost

reduction and performance optimization at large scale by utilizing existing infrastructure and techniques.

Conclusion

The spheroidization process has a significant impact on graphite in terms of both agglomerate morphology and the graphite structure itself. In this work, we present new insights into the effect of the spheroidization conditions on the graphite particle characteristics and their impact on electrochemical behaviour. We demonstrate that the choice of the spheroidization parameters not only affect the particle shape, density and surface area, but several other particle properties as well, such as the particle and crystallite dimension, and the surface chemical and physical composition. Many of these properties are highly influenced by each other, and the optimization of the spheroidization conditions necessitates the understanding and evaluation of several characteristics of the carbon and their impact on the overall electrochemical behaviour. High energy conditions result in increasing disorder (which may be attributed to increasing defects), as seen from the Raman, N₂ physisorption, and O₂ chemisorption analyses. Our results show that the electrochemical response of anodes made with graphite shaped under relatively high-energy corresponds to faster kinetics and less side-reactions (e.g., lithium depositions) when charged at high current rates, compared with anodes made with graphite spheroidized with lower energy impact. We demonstrate that the impact of the fast-charge ability

revealed for thin electrodes in half-cells is retained in realistic applications in pouch-cells with standard (NCM) cathode. This work, therefore, offers a basis for better understanding of state-of-art graphite production, which can be transferred to a more general context to define key parameters to be controlled and characterization methodologies for design of graphite for LiBs applications. Moreover, the trends revealed here are highly significant for current graphite production, as they can be transferred to a larger scale and support development of fast-charging LiBs. In this way, this represents an important basis for future graphite research – particularly with respect to areas of rapid LiB development.

Experimental Section

Graphite shaping and characterization

Graphit Kropfmühl GmbH supplied the pristine materials as purified (carbon content > 99.85 wt.%) crystalline natural graphite (NG) flakes. Spheroidization was carried out using high-speed rotational dry impact mill (Hybridizer, type NHS-0, Nara Machinery Co.) described elsewhere, to give two samples: NG1 (9000 rpm, 25 g batch and 4 min milling time) and NG2 (11000 rpm, 10 g batch and 8 min milling time).^[22] The particle size distribution of the two samples has been adjusted by removing the coarse fraction (>40 µm) with an air jet sieve e200 LS instrument (Hosokawa Alpine AG) and of the fine particles (<8 µm) via air-classification by using a Picoline multi-process mill equipped with a Picosplit 20 ATP classifier module (Hosokawa Alpine AG). The volume-based particle size distribution of the samples was measured by laser diffraction with a Mastersizer Micro particle size analyzer (Malvern Instruments GmbH). Scanning electron microscopy (SEM) images were recorded using a Zeiss instrument LEO Gemini 1530 VP. The bulk density was calculated by measuring the weight of the powder sample occupying a fixed volume (100 mL cylinder). The tap density of the graphite samples was determined by mechanically tapping the sample powder for 2500 times in a 100 mL cylinder with a STAV 2003 (J. Engelsmann AG) jolting volumeter. Nitrogen physisorption measurements were performed with a 3Flex 3500 instrument (Micromeritics Instrument Corp.) at 77 °K (Figure S1 in Supplementary Information) to analyze the specific surface area (BET-SSA) and surface heterogeneity. Raman spectra were collected with a SENTERRA Raman Microscope (Bruker Optik GmbH) using a 532 nm laser (10 mW, Rayleigh-filter). Background correction was performed using the software OPUS (Bruker Optik GmbH) and peaks were fitted using a Voigt-Function in OriginLab software (Figures S2, S3 and S4 in Supporting Information). The intensity ratio of the Raman bands, I_D/I_G , was calculated based on the area of the fitted peak for the G- and D-band of the Raman spectra recorded for the different graphite samples. The crystallite size L_a was calculated using the equation described in literature.^[58] Oxygen chemisorption and temperature-programmed-desorption (TPD) measurements were undertaken using a 3Flex 3500 instrument based on the procedure described in literature.^[46] The sample was heated to 300 °C under oxygen flow and kept at this temperature for 12 h. Afterwards, TPD measurements were performed under continuous He flow by heating the sample up to 1000 °C. The desorbed gas species were detected with a mass spectrometer (Cirrus 2, MKS instruments) connected to the instrument. It is worth noting that the BET surface area of commercially available graphite samples is generally reduced, typically with carbon particle coating, to minimize the irreversible capacity loss due to electrolyte decomposition (SEI formation). However, in order to study in detail the link between spheroidization conditions and surface characteristics of the particles, and directly

correlate them with the electrochemical performance, no further surface post-treatment is performed in this work.

Electrochemical measurements

After sieving and classification, electrodes were prepared from the graphite powders using commercially available water-soluble binders (carboxymethylcellulose Sunrose MAC500 from Nippon Paper Industries Co., Ltd. and TRD2001 from JSR Micro NV, in the ratio 1:1), and carbon black (Super P Li, Imerys Graphite & Carbon) as conductive additive. The final electrode composition was 94 wt.% of active material, 2 wt.% carbon black and 4 wt.% binder. The slurries were coated on a copper foil (Schlenk AG, thickness 12 µm) current collector by using lab-scale coating equipment (Erichsen). By setting different coating thicknesses of the doctor blade, we obtained two different active material areal loadings: ca. 3 mg cm⁻² (thin electrodes) and 7.6–7.8 mg cm⁻² (standard electrodes). The density of the latter electrodes was then increased to 1.4 g cm⁻³ by using a lab calander (CA5/250 from Sumet-Messtechnik).

Half-cell measurements: circular electrodes (12 mm diameter) were cut and dried under vacuum at 120 °C. The half-cell measurements were performed in 3-electrode set-up (T-cells) by using 3 glass fiber layers (Whatman GF/A) as separator, and lithium discs (Alpha Aesar) as the counter electrode and pseudo-reference electrode. The electrolyte used for electrochemical test is 1 M LiPF₆ in EC:EMC (3:7 wt.) + 2 wt.% VC (Ube Industries, LTD). The formation of the half-cells was performed by cycling between 0.02 and 1.5 V vs. Li/Li⁺ at the rate of 0.1 C (1 C = 372 mA g⁻¹). After formation, the cells were tested by applying a constant current (CC step, current ranging from 0.1 C to 5 C, 3 or 5 cycles at each current) during graphite reduction (lithiation) and maintaining the cut-off voltage of 0.02 V vs. Li/Li⁺ (CV) until the measured current was below 0.05 C (no time limitation). Subsequent graphite de-lithiation was performed by applying a constant current of 0.2 C up to the voltage cut-off of 1.5 V vs. Li/Li⁺.

Full-cell measurements: the calandered electrodes with standard active material loadings were punched (26 cm²) and dried under vacuum at 120 °C. Single-layer pouch-cells were assembled in dry-room by using a standard NCM-based cathode (electrodes prepared at ZSW from commercially available Lithium Nickel Cobalt Manganese Oxide NCM₅₂₃, cutting area 23.94 cm²), Celgard H1609 as separator, and 1 M LiPF₆ EC:DMC (3:7 wt.) + 2 wt.% VC (Ube Industries, LTD) as electrolyte. The pouch cells were clamped in a holding device made of Plexiglas plates (applied pressure ca. 4 N cm⁻²). The formation of the pouch-cells was performed by cycling 5 times between 3 and 4.2 V at the rate of 0.1 C. After formation, the electrochemical tests for fast-charging investigation were performed by CCCV charge using current rates ranging from 0.2 C to 2.5 C (limit current for CV duration of 0.05 C). Discharge was always performed at 0.2 C rate. The long-term cycling stability tests were performed by CCCV charge (charging current 0.5 C, limit current for CV duration of 0.05 C) and CC discharge at 0.2 C rate. All pouch-cells were assembled by using anode/cathode capacity ratio in the range 1.11 to 1.13.

All electrochemical measurements were performed in a thermal chamber at a temperature of 25 °C. All tests have been repeated at least twice to confirm the reproducibility of the results.

Acknowledgements

The authors are grateful to Graphit Kropfmühl GmbH for providing the graphite raw materials, to Dr. C. Pfeifer (ZSW) for the SEM images and to Dr. A. Hoffmann (ZSW) for providing the cathode. We also acknowledge the BMBF (Federal Ministry of

Education and Research, Germany) for the funding projects RONDO (03XP0112E) and Oekobat-2020 (03XP0033F).

Conflict of Interest

The authors declare no conflict of interest.

Data Availability Statement

Research data are not shared.

Keywords: fast-charge · graphite anode · lithium-ion batteries · natural graphite spheroidization · surface functionalities

- [1] C. Pillot, The Rechargeable Battery Market, value chain and Main Trends 2020–2030, AABC 2021 (Virtual), 2021-01–20.
- [2] Z. Du, D. L. Wood III, I. Belharouak, *Electrochem. Commun.* **2019**, *103*, 109–113.
- [3] a) H. Buqa, D. Goers, M. Holzapfel, M. E. Spahr, P. Novák, *J. Electrochem. Soc.* **2005**, *152* (2), A474-A481; b) D. Parikh, T. Christensen, J. Li, *J. Power Sources* **2020**, *474*, 228601.
- [4] D. Parikh, T. Christensen, C.-Te Hsieh, J. Li, *J. Electrochem. Soc.* **2019**, *166* (14), A3377-A3383.
- [5] K. S. N. Vikrant, S. Allu, *J. Electrochem. Soc.* **2021**, *168*, 020536.
- [6] T. A. Pham, K. E. Kweon, A. Samanta, M. T. Ong, V. Lordi, J. E. Pask, *J. Phys. Chem. C* **2020**, *124*, 21985–21992.
- [7] T. Abe, H. Fukuda, Y. Iriyama, Z. Ogumi, *J. Electrochem. Soc.* **2004**, *151*, A1120-A1123.
- [8] K. G. Gallagher, S. E. Trask, C. Bauer, T. Woehrle, S. F. Lux, M. Tschech, P. Lamp, B. J. Polzin, S. Ha, B. Long, Q. Wu, W. Lu, D. W. Dees, A. N. Jansen, *J. Electrochem. Soc.* **2016**, *163*, A138-A149.
- [9] W. Cai, Y.-X. Yao, G.-L. Zhu, C. Yan, L.-L. Jiang, C. He, J.-Q. Huang, Q. Zhang, *Chem. Soc. Rev.* **2020**, *49*, 3806–3833.
- [10] J. Asenbauer, T. Eisenmann, M. Kuenzel, A. Kazzazi, Z. Chen, D. Bresser, *Sustainable Energy & Fuels* **2020**, *4*, 5387–5416; *Fuels* **2020**, *4*, 5387–5416.
- [11] T. Al-Ani, S. Leinonen, T. Ahtola, D. Salvador, *Minerals* **2020**, *10*, 680.
- [12] J.-S. Park, M.-H. Lee, I.-Y. Jeon, H.-S. Park, J.-B. Baek, H.-K. Song, *ACS Nano* **2012**, *6*, 12, 10770–10775.
- [13] Q. Cheng, R. Yuge, K. Nakahara, N. Tamura, S. Miyamoto, *J. Power Sources* **2015**, *284*, 258–263.
- [14] J.-H. Shim, S. Lee, *J. Power Sources* **2016**, *324*, 475–483.
- [15] Q. Cheng, Y. Zhang, *J. Electrochem. Soc.* **2018**, *165* (5), A1104-A1109.
- [16] J. Billaud, F. Bouville, T. Magrini, C. Villevieille, A. R. Studart, *Nat Energy* **2016**, *1*, 16097.
- [17] M. Mancini, F. Nobili, S. Dsoke, F. D'Amico, R. Tossici, F. Croce, R. Marassi, *J. Power Sources* **2009**, *190*, 141–148.
- [18] F. Nobili, S. Dsoke, M. Mancini, R. Tossici, R. Marassi, *J. Power Sources* **2008**, *180*, 845–851.
- [19] M. E. Spahr, Verfahren zur Herstellung von Graphitpulvern mit erhöhter Schüttdichte, EP 1240103 B1, 2007.
- [20] K. Ohzeki, Y. Saito, B. Golman, K. Shinohara, *Carbon* **2005**, *43*, 1673–1679.
- [21] F. Dismal, L. Aymard, L. Dupont, J.-M. Tarascon, *J. Electrochem. Soc.* **1996**, *143*, 3959–3972.
- [22] I. Ruggeri, J. Martin, M. Wohlfahrt-Mehrens, M. Mancini, *J. Solid State Electrochem.* **2022**, *26*, 73–83.
- [23] M. Mundzinger, S. Farsi, M. Rapp, U. Golla-Schindler, U. Kaiser, M. Wachtler, *Carbon* **2017**, *111*, 764–773.
- [24] C. Natarajan, H. Fujimoto, A. Mabuchi, K. Tokumitsu, T. Kasuh, *J. Power Sources* **2001**, *92*, 187–192.
- [25] H. Wang, T. Ikeda, K. Fukuda, M. Yoshio, *J. Power Sources* **1999**, *83*, 141–147.
- [26] A. C. Ferrari, *Solid State Comm.* **2007**, *143*, 47–57.
- [27] M. A. Pimenta, G. Dresselhaus, M. S. Dresselhaus, L. G. Cançado, A. Jorio, R. Saito, *Phys. Chem. Chem. Phys.: PCCP* **2007**, *9*, 1276–1291.
- [28] M. S. Dresselhaus, A. Jorio, R. Saito, *Annu. Rev. Condens. Matter Phys.* **2010**, *1*, 89–108.
- [29] S. Reich, C. Thomsen, *Philosophical Transactions. Series A, Mathematical, Physical and Engineering Sciences* **2004**, *362*, 2271–2288.
- [30] K. Sato, R. Saito, Y. Oyama, J. Jiang, L. G. Cançado, M. A. Pimenta, A. Jorio, G. G. Samsonidze, G. Dresselhaus, M. S. Dresselhaus, *Chem. Phys. Lett.* **2006**, *427*, 117–121.
- [31] F. Tuinstra, J. L. Koenig, *J. Chem. Phys.* **1970**, *53*, 1126–1130.
- [32] A. C. Ferrari, J. Robertson, *Philosophical Transactions. Series A, Mathematical, Physical and Engineering Sciences* **2004**, *362*, 2477–2512.
- [33] T. Xing, L. H. Li, L. Hou, X. Hu, S. Zhou, R. Peter, M. Petracic, Y. Chen, *Carbon* **2013**, *57*, 515–519.
- [34] J. M. Mendoza-Duarte, M. H. Bocanegra-Bernal, R. Martinez-Sanchez, I. Estrada-Guel, *Microscop. Microanal. (Suppl 2)* **2013**, *19*, 1596–1597.
- [35] K. Niwase, T. Tanaka, Y. Kakimoto, K. N. Ishihara, P. H. Shingu, *Materials Transactions JIM* **1995**, *36*, 282–288.
- [36] a) J. P. Olivier, *J. Porous Materials* **1995**, *2*, 9–17; b) J. P. Oliver, *Fifth International Conference on the Fundamentals of Adsorption* **1995**, Pacific Grove, CA; c) J. P. Oliver in *Adsorption by Carbons*, ed. by E. J. Bottani, J. M. D. Tascón, Elsevier Science & Technology, Chapter 7, 2008.
- [37] J. P. Olivier, M. Winter, *J. Power Sources* **2001**, *97*–98, 151–155.
- [38] P. Bernardo, J. Dentzer, R. Gadiou, W. Märkle, D. Goers, P. Novák, M. E. Spahr, C. Vix-Guterl, *Carbon* **2011**, *49*, 4867–4876.
- [39] U. Zielke, K. J. Hüttlinger, W. P. Hoffman, *Carbon* **1996**, *34*, 983–998.
- [40] J. L. Figueiredo, M. F. R. Pereira, M. M. A. Freitas, J. J. M. Órfão, *Carbon* **1999**, *37*, 1379–1389.
- [41] Y. Otake, R. G. Jenkins, *Carbon* **1993**, *31*, 109–121.
- [42] Q.-L. Zhuang, T. Kyotani, A. Tomita *Energy & Fuels* **1994**, *8*, 714–718.
- [43] Q.-L. Zhuang, T. Kyotani, A. Tomita *Carbon* **1994**, *32*, 539–540.
- [44] B. Marchon, J. Carrazza, H. Heinemann, G. A. Somorjai, *Carbon* **1988**, *26*, 507–514.
- [45] J. R. Dahn, T. Zheng, Y. Liu, J. S. Xue, *Science* **1995**, *270*, 590–593.
- [46] M. E. Spahr, H. Buqa, A. Würsig, D. Goers, L. Hardwick, P. Novák, F. Krumeich, J. Dentzer, C. Vix-Guterl, *J. Power Sources* **2006**, *153*, 300–311.
- [47] A. Funabiki, M. Inaba, Z. Ogumi, *J. Power Sources* **1997**, *68*, 227–231.
- [48] N. Ogihara, Y. Itou, T. Sasaki, Y. Takeuchi, *J. Phys. Chem. C* **2015**, *119*, 4612–4619.
- [49] S. J. An, J. Li, C. Daniel, D. Mohanty, S. Nagpure, D. L. Wood III, *Carbon* **2016**, *105*, 52–76.
- [50] S. H. Ng, C. Vix-Guterl, Ph. Bernardo, J. Dentzer, R. Gadiou, M. E. Spahr, D. Goers, *Carbon* **2009**, *47*, 705–712.
- [51] T. R. Tanim, E. J. Dufek, C. C. Dickerson, S. M. Wood, *J. Electrochem. Soc.* **2019**, *166* (12), A2689-A2696.
- [52] C. Uhlmann, J. Illig, M. Ender, R. Schuster, E. Ivers-Tiffée, *J. Power Sources* **2015**, *279*, 428–438.
- [53] I. D. Campbell, M. Marzook, M. Marinescu, G. J. Offer, *J. Electrochem. Soc.* **2019**, *166* (4), A725-A739.
- [54] T. Waldmann, B.-I. Hogg, M. Wohlfahrt-Mehrens, *J. Power Sources* **2018**, *384*, 107–124.
- [55] Z. Li, J. Huang, B. Y. Liaw, V. Metzler, J. Zhang, *J. Power Sources* **2014**, *254*, 168–182.
- [56] U. Janakiraman, T. R. Garrick, M. E. Fortier, *J. Electrochem. Soc.* **2020**, *167*, 160552.
- [57] D. E. Brown, E. J. McShane, Z. M. Konz, K. B. Knudsen, B. D. McCloskey, *Cell Reports Physical Science* **2021**, *2*, 100589.
- [58] L. G. Cançado, K. Takai, T. Enoki, M. Endo, Y. A. Kim, H. Mizusaki, A. Jorio, L. N. Coelho, R. Magalhães-Paniago, M. A. Pimenta, *Appl. Phys. Lett.* **2006**, *88*, 163106–1–63106–3.

Manuscript received: March 7, 2022

Accepted manuscript online: March 11, 2022

Version of record online: April 6, 2022